

**A TWO-WAY COUPLED MODEL OF VISCO-THERMO-ACOUSTIC EFFECTS IN PHOTOACOUSTIC TRACE GAS SENSORS\***ALI MOZUMDER<sup>†</sup>, ARTUR SAFIN<sup>‡</sup>, SUSAN E. MINKOFF<sup>†</sup>, AND JOHN ZWECK<sup>†</sup>

**Abstract.** We introduce the first two-way coupled model for the thermo-viscous damping of a mechanical structure (such as quartz tuning fork) that is forced by the weak acoustic and thermal waves generated when a laser source periodically interacts with a trace gas. The model is based on a Helmholtz system of thermo-visco-acoustic equations in the fluid, together with a system of equations for the temperature and the displacement of the structure. These two subsystems are coupled across the fluid-structure interface via several conditions. With this model, the user specifies the geometry of the structure and the viscous and thermal parameters of the fluid, and the model outputs an effective damping parameter and a signal strength that is proportional to the concentration of the trace gas. This new model is a significant improvement over existing one-way coupled models in which damping effects are incorporated via a priori laboratory measurements. Analytical solutions derived for an annular structure show reasonable agreement between the one-way and two-way coupled models at higher ambient pressures. However, at low ambient pressure the one-way coupled model does not adequately capture thermo-viscous effects.

**Key words.** trace-gas sensors, photoacoustic spectroscopy, visco-thermo-acoustics, viscous damping, two-way coupled models

**MSC codes.** 35J05, 35K05, 35Q35

**DOI.** 10.1137/21M1447659

**1. Introduction.** In this paper we introduce a two-way coupled model for the resonant vibration of a mechanical structure that is forced by a thermo-acoustic wave in a viscous fluid. We developed this model to improve upon more commonly used one-way coupled models for photoacoustic trace gas sensors that employ a quartz tuning fork (QTF) to detect the weak acoustic and thermal waves generated when a modulated laser interacts with a trace gas. The new model incorporates viscous damping for sensors with arbitrary geometry, thus avoiding the need for a priori laboratory measurements of the effective damping in particular tuning forks.

Quartz Enhanced Photoacoustic Spectroscopy (QEPAS) [21, 42] is a trace gas sensing technique for the detection of harmful gases such as carbon monoxide in industrial workplaces, environmental pollutants such as ammonia, and greenhouse gases such as carbon dioxide. The diagnosis of diseases is also expected to benefit from breath analyzers that will replace or supplement invasive blood testing and biopsies [29, 41]. Large-scale adoption of such trace gas sensors requires systems that are compact, portable, efficient, sensitive, spectrally selective, cost-effective, and highly reliable. QEPAS sensors have many of these characteristics [42]. In particular, they can be as small as several cubic millimeters, whereas sensors based on other sensitive spectroscopic techniques require large cell volumes of tens to hundreds of cubic

---

\*Received by the editors September 21, 2021; accepted for publication (in revised form) December 20, 2022; published electronically June 2, 2023.

<https://doi.org/10.1137/21M1447659>

**Funding:** This work was supported by the National Science Foundation under grant DMS-1620293.

<sup>†</sup>Department of Mathematical Sciences, University of Texas at Dallas, Richardson, TX 75080 USA (axm164531@utdallas.edu, sminkoff@utdallas.edu, zweck@utdallas.edu).

<sup>‡</sup>Eawag: Swiss Federal Institute of Aquatic Science and Technology, CH-8600 Dübendorf, Switzerland (asafin@gmail.com).

centimeters. Although the modeling of trace gas sensors is our primary motivation, the two-way coupled model introduced in this paper may be useful for other applications that involve interactions between thermo-visco-acoustic fluids and mechanical structures. Examples of such applications include the study of thermal phenomena near thin bodies [26], the design of hearing aid transducers and micro-electrical-mechanical devices [10], and highly sensitive chemical sensors based on microcantilevers that can sense mass changes in the picogram range due to chemical reactions [11].

With photoacoustic spectroscopy, when optical radiation from a laser is absorbed by a trace gas, the gas molecules release their excess vibrational energy in the form of heat. By sinusoidally modulating the interaction between the laser radiation and the trace gas, a thermal diffusion wave is generated in the fluid. In addition, vibrational-to-translational energy conversion processes at the molecular level generate an acoustic pressure wave. In a QEPAS sensor, the acoustic pressure wave induces a mechanical vibration of a quartz tuning fork (QTF), which is in turn converted to an electric current via the piezoelectric effect in quartz. Even though the acoustic wave is extremely weak, the QTF has a sharp resonance that significantly amplifies the signal. Therefore, the piezoelectric current can be detected by choosing the modulation frequency of the laser to precisely agree with a resonance frequency of the QTF vibration. Since the entire process is linear, the amplitude of the received electrical signal is proportional to the concentration of the trace gas. QEPAS sensors often also include a microresonator that further increases sensitivity by amplifying the acoustic pressure wave by a factor of about thirty [12]. If the ambient pressure is sufficiently low and the laser source is positioned close enough to the QTF, the thermal diffusion wave can dominate the acoustic pressure wave on the surface of the QTF. In this situation, the QTF directly detects the thermal wave in a process called Resonant OptoThermoAcoustic DEtection (ROTADE) [22, 35]. Since the lines in the absorption spectrum become more distinct as the ambient pressure is lowered, ROTADE sensors provide more wavelength selectivity than do QEPAS sensors. Recent experimental research on QEPAS sensors has been focused on increasing sensitivity by using custom-made tuning forks with different geometric parameters and employing novel experimental designs such as aligning the laser beam close to one tine of the tuning fork, or using two lasers, each with their own microresonator [13, 27, 33].

Current analytical and computational models of QEPAS and ROTADE systems involve one-way coupling from fluid variables to the structural displacement [3, 15, 34, 35, 39]. Damping effects are incorporated into the model in an ad hoc manner that requires a priori laboratory measurements of the *Q*-factor of the system. To experimentally determine the *Q*-factor, the driving frequency,  $\omega$ , is varied about the undamped (vacuum) resonance frequency,  $\omega_0$ , and the output electrical current is measured as a function of  $\omega$  [24]. The resulting resonance curve is narrower when the damping is smaller. The *Q*-factor is then defined in terms of the resonance curve using the formula

$$(1.1) \quad Q = \frac{\omega_0}{\Delta\omega_{\sqrt{2}}},$$

where  $\Delta\omega_{\sqrt{2}}$  denotes the full width at  $1/\sqrt{2}$  of the maximum value of the resonance. For one-way coupled models, good agreement has been obtained with experimental systems for which the *Q*-factor is known and which are operated at higher ambient pressure values. However, it has not been possible to obtain agreement when visco-thermal effects play a more prominent role, such as when the QTF and microresonator are in close proximity to each other or the system is operated at low ambient pressures

[14, 39]. Most importantly, one-way coupled numerical models do not allow for the optimization of the sensitivity of the sensor as a function of QTF geometry.

To address these deficiencies, experimentalists have gathered data from a wide range of tuning fork designs, and theoreticians have developed analytical formulae for the  $Q$ -factors of cantilevers and tuning forks. Specifically, via experimental analysis Patimisco et al. [32] developed rules that indicate how the  $Q$ -factor varies as the dimensions of the tuning fork change. The main source of damping in a QTF is viscous damping due to the motion of the tines through the viscous fluid [31]. Aoust et al. [1] derived an analytical formula for the  $Q$ -factor due to viscous damping in terms of the fluid density and viscosity and the geometric and mechanical parameters of the QTF. Despite making several simplifying assumptions, they obtained good agreement with experimentally measured  $Q$ -factors over a wide range of ambient pressures.

In this paper we introduce the first two-way coupled model for both QEPAS and ROTADE sensors that more realistically incorporates the effects of viscous damping. The model is based on systems of Helmholtz equations for the acoustic pressure, temperature, and velocity in the fluid, as well as the temperature and displacement of the structure coupled via conditions on the fluid-structure interface. With this approach, the user specifies the geometry of the structure and the viscous and thermal parameters of the fluid, while the  $Q$ -factor and signal strength are both outputs of the model. Consequently, one can accurately model arbitrary tuning forks and novel geometric configurations including the case in which the QTF and microresonator are in close proximity to each other.

The two-way coupled model is based on a system of equations originally derived by Morse and Ingard [30] for the temperature, pressure, and velocity of the fluid, together with standard equations for the temperature and displacement of the structure. Cao and Diebold [7] derived a spherically symmetric analytical solution to the pressure-temperature subsystem of the Morse–Ingard equations in their study of the effects that heat conduction and fluid viscosity have on the acoustic wave produced by laser irradiation of a water droplet. Using a different approach, Kaderli et al. [18] derived an analytical solution for the pressure-temperature subsystem in a special case with cylindrical symmetry, which they used to study how the interaction between the pressure and temperature near a fluid-structure interface gives rise to a thermal boundary layer that affects the diffusion of heat into the structure. Kaderli et al. showed that near the interface, the temperature in the structure can be at least an order of magnitude larger than that computed using a simpler model in which the temperature in the fluid is governed by the heat equation. However, they did not model the temperature and displacement of the structure to investigate the effect that the thermal boundary layer has on the sensor performance.

Brennan and Kirby [5] established the coercivity and well-posedness of the pressure-temperature subsystem and proved optimal error estimates for standard Galerkin finite elements. They also presented a data-dependent block preconditioner with superior performance over classical preconditioning techniques such as the block Jacobi and Gauss–Seidel methods. By slightly reformulating the pressure-temperature subsystem, Kirby and Coogan [19] rigorously established an eigenvalue clustering result for the associated block preconditioners. They obtained mesh-independent results that in practice require many fewer iterations than are required for the system studied in [5]. Safin, Minkoff, and Zweck [38, 39] moved beyond the pressure-temperature system in the fluid by proposing a one-way coupled model in which the fluid pressure and the temperature variation in the QTF drive the deformation of the QTF, and ad hoc damping is incorporated using experimentally measured values of the  $Q$ -factor

of the QTF. By solving the equations using the finite element method and a custom preconditioner, they were able to compare the results of their numerical simulations to experimental results of Kosterev and Doty (see [22, 23]), who measured how the piezoelectric signal varies with respect to the position of the laser beam. At high ambient pressure, they obtained excellent agreement between the numerical and experimental results, with at most a 10% discrepancy in regions with strong signal. However, at low ambient pressure, they were only able to obtain quantitative agreement with experiments by normalizing the contributions due to the acoustic and thermal components of the signal. The results we present here suggest that this deficiency with the one-way model at low ambient pressure is likely due to the manner in which damping was implemented.

To increase understanding of the coupling mechanisms in the two-way model, we derive an analytical solution to the model in the special case that the structure is a two-dimensional annulus instead of a QTF. Although the annular geometry is quite different from that of the QTF in a trace gas sensor, the numerical results we obtain shed light on the differences between the damping effects obtained when using the one-way and two-way coupled models. By computing the ad hoc damping parameter in the one-way model from the resonance curve for the displacement of the structure we can compare the signal strengths obtained using the two models. Our numerical results confirm that the one-way coupled model does not adequately capture viscous damping effects in regimes where visco-thermal effects play a more prominent role. These results provide further impetus for the development of more efficient numerical methods for the two-way coupled model.

In section 2 we briefly review the one-way coupled model previously introduced by Safin, Zweck, and Minkoff [39] and formulate the two-way coupled model. In section 3 we derive an analytic solution of the two-way coupled model in a special case in which the structure is an annulus. In section 4 we present the numerical results obtained in the special case of annular geometry, using both the analytical solution and a finite-element implementation that we discuss in the appendix.

**2. Mathematical model.** In subsection 2.2, we introduce the first two-way coupled model for a photoacoustic trace gas sensor that uses a QTF to detect the weak visco-thermo-acoustic wave generated by the periodic interaction between a laser heat source and a trace gas. With this model, temperature and pressure fluctuations in the fluid are coupled to the elastic deformation of the mechanical structure via conditions imposed on the fluid-structure interface. The two-way coupled model is an improvement over previous one-way models [15, 34, 39] in which there was no feedback from the structure to the fluid. In subsection 2.1 we briefly describe the one-way coupled model developed by Safin, Zweck, and Minkoff [39] which we build on for the two-way coupled model.

We formulate both models in terms of a fluid domain,  $\Omega_F$ , and a structural domain,  $\Omega_S$ . We decompose the boundary of the structural domain as  $\partial\Omega_S = \partial\Omega_S^{\text{Free}} \cup \partial\Omega_S^{\text{Fixed}}$ , where  $\partial\Omega_S^{\text{Free}}$  is the portion of the boundary that is free to vibrate and  $\partial\Omega_S^{\text{Fixed}}$  is the portion that is clamped. We let  $\partial\Omega_{FS}$  denote the fluid-structure interface. For the numerical results in this paper, we choose the fluid domain to be a two-dimensional disc of radius,  $R_1$ , and the structural domain to be an annulus with inner radius,  $R_1$ , and outer radius,  $R_2$  (see Figure 1). The inner boundary of the annulus is free to vibrate and the outer portion is fixed. A radially symmetric source function is positioned at the center of the disc. For QEPAS and ROTADE sensors, the concentration of the trace gas is proportional to the amplitude of vibration of

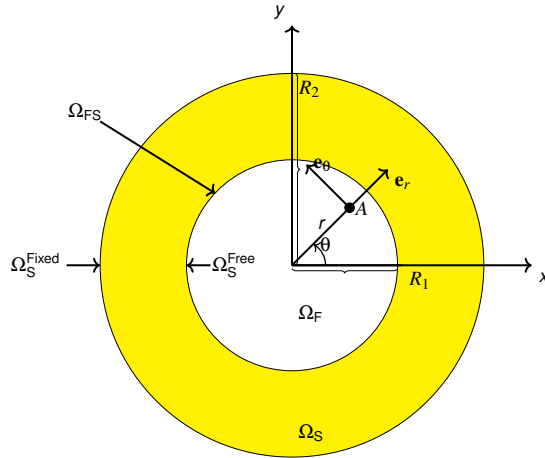


FIG. 1. *Cross section of a cylindrical fluid domain (white disc),  $\Omega_F$ , surrounded by an annular structural domain (yellow),  $\Omega_S$ . (Color figure available online.)*

the tip of a tine of the tuning fork [34]. Similarly, for the annular geometry, we define the output signal to be the amplitude of vibration of the inner boundary of the annulus. Although this geometric configuration does not correspond to that of an experimental trace gas sensor, the symmetry of the problem allows us to derive an analytical solution of the model. We stress that the formulation of the model is independent of the geometry of the structure, and in particular can be readily adapted to the tuning fork geometry of QEPAS and ROTADE sensors.

**2.1. One-way coupled model.** In this section, we summarize the one-way coupled model of Safin, Zweck, and Minkoff [39] for the pressure and temperature in the fluid and the induced elastic deformation of a mechanical structure such as a QTF.

The periodic interaction between laser radiation and a trace gas induces a disturbance in the ambient fluid in which the thermodynamic variables fluctuate about their equilibrium values. We model the variations of the temperature, pressure, and velocity of the fluid using a coupled system of equations derived by Morse and Ingard [30, p. 282] that incorporates the effects of thermal diffusion and fluid viscosity. We employ a formulation of these equations in which the temperature,  $\tau_F$ , and pressure,  $p$ , satisfy a coupled subsystem. Because the heat source is time harmonic, we consider the Helmholtz form of the model in which all functions are of the form  $f(\mathbf{x}, t) = \Re[f(\mathbf{x})e^{-i\omega t}]$ , where  $\mathbf{x}$  is position, and all time derivatives are given by multiplication by  $-i\omega$ . Then, the pressure-temperature equations are given by

$$(2.1) \quad \Omega \Delta \tau_F + i \left( \frac{\omega}{c} \right)^2 \left( \tau_F - \frac{\gamma - 1}{\gamma \alpha} p \right) = -\frac{\omega}{c^2} S,$$

$$(2.2) \quad \Delta p + \frac{\gamma}{c^2} (\omega^2 - i c^2 \Lambda \Delta) (p - \alpha \tau_F) = 0.$$

Here  $\omega$  is the laser modulation frequency,  $c$  is the speed of sound,  $\gamma$  is the isentropic expansion factor of the gas,  $\alpha$  is the rate of change of pressure with respect to temperature at constant volume,  $\Omega = \omega \ell_h / c$ , where  $\ell_h = K_F / (\rho_F c C_p)$  is the characteristic length of heat conduction, and  $\Lambda = \omega \ell_v / c$ , where  $\ell_v = (\eta_F + \frac{4}{3} \mu_F) / (\rho_F c)$  is the characteristic length of viscosity. Here,  $\rho_F$  is the density of the fluid,  $\mu_F$  is the dynamic

viscosity,  $\eta_F$  is the bulk viscosity,  $K_F$  is the thermal conductivity of the fluid, and  $C_p$  is the specific heat capacity of the fluid. If the frequency,  $\omega$ , is on the order of  $10^5$ , as is typically the case for a QTF, the parameters  $\Omega$  and  $\Lambda$  are on the order of  $10^{-5}$ .

The photoacoustic heat source,  $S$ , on the right-hand side of (2.1) is given by  $S = H/(\rho_F C_p)$ , where  $H$  is the heat power density deposited into the gas [28]. We model the laser as a Gaussian beam so that

$$(2.3) \quad S = \frac{\alpha_{\text{eff,ref}} R_0 T_0}{P_{\text{ref}} C_p} \frac{W_L}{4\pi\sigma^2} e^{-r^2/2\sigma^2},$$

where  $r$  is the radial distance from the axis of the beam,  $\sigma$  is the beam width,  $W_L$  is the laser power,  $R_0$  is the ideal gas constant,  $T_0$  is the ambient temperature, and  $\alpha_{\text{eff,ref}}$  is the absorption coefficient at ambient pressure,  $P_{\text{ref}}$ .<sup>1</sup>

Next, we discuss the equations for the temperature and elastic deformation of the mechanical structure and the fluid-structure interface conditions. With the one-way coupled model we impose the interface condition

$$(2.4) \quad \nabla p \cdot \mathbf{n} = 0 \quad \text{on } \partial\Omega_{\text{FS}},$$

where  $\mathbf{n}$  is a normal vector field on the fluid-structure interface. At the interface, the acoustic pressure induces a mechanical vibration of the structure. Furthermore, the heat generated by the interaction between the laser radiation and the trace gas molecules dissipates into the interior of the structure inducing a thermal stress which results in an additional thermo-elastic deformation of the structure.<sup>2</sup>

The Helmholtz form of the heat equation for the temperature,  $\tau_S$ , in the structure,  $\Omega_S$ , is given by

$$(2.5) \quad i\omega\tau_S + D_S\Delta\tau_S = 0,$$

where  $D_S = K_S/\rho_S C_{p,S}$  is the diffusion constant. Here  $K_S$  is the thermal conductivity,  $\rho_S$  is the density, and  $C_{p,S}$  is the specific heat capacity of the structure. On the fluid-structure interface we impose the standard conditions

$$(2.6) \quad \tau_S = \tau_F \quad \text{on } \partial\Omega_{\text{FS}},$$

$$(2.7) \quad K_S \nabla \tau_S \cdot \mathbf{n} = K_F \nabla \tau_F \cdot \mathbf{n} \quad \text{on } \partial\Omega_{\text{FS}}.$$

The stress tensor,  $\boldsymbol{\sigma}_S$ , in a thermoelastic material,  $\Omega_S$ , is given by [8, pp. 310–326]

$$(2.8) \quad \boldsymbol{\sigma}_S = \mathbf{C}[\boldsymbol{\epsilon}_S] - \mathbf{C}[\boldsymbol{\alpha}_S \tau_S],$$

where  $\mathbf{C}$  is the elasticity tensor that relates the strain tensor,  $\boldsymbol{\epsilon}_S$ , of the structure to the applied stress, and  $\boldsymbol{\alpha}_S$  is the thermal expansion tensor, which quantifies the change in volume of the material when it is heated in the absence of stress. Since the displacement,  $\mathbf{u}$ , of the structure is small, we may assume that  $\mathbf{C}[\boldsymbol{\epsilon}_S] = \mathbf{C}[\nabla \mathbf{u}]$ . Under this assumption, the equation for the displacement of the structure is given by

$$(2.9) \quad \nabla \cdot \mathbf{C}[\nabla \mathbf{u}] + (\rho_S \omega^2 - i\omega\delta_S) \mathbf{u} = \nabla \cdot \mathbf{C}[\boldsymbol{\alpha}_S \tau_S] \quad \text{in } \Omega_S.$$

---

<sup>1</sup>Since the dependence of  $S$  on the ambient pressure has not been discussed in the literature, we provide a derivation of (2.3) in the supplementary material (suppmats.pdf [local/web 228KB]).

<sup>2</sup>In a QEPAS sensor the output signal is primarily due to the pressure, while in a ROTADE sensor it is primarily due to the temperature.

Here, we have incorporated damping with the addition of the ad hoc term,  $i\omega\delta_S \mathbf{u}$ . The interface condition on the structure due to the fluid is given by

$$(2.10) \quad (\mathbf{C}[\nabla \mathbf{u}] - \mathbf{C}[\alpha_S \tau_S]) \mathbf{n} = -p \mathbf{n} \quad \text{on } \partial\Omega_S^{\text{Free}}.$$

We also assume that  $\mathbf{u} = \mathbf{0}$  and  $\nabla \mathbf{u} = \mathbf{0}$  on  $\partial\Omega_S^{\text{Fixed}}$ .

As in Petra et al. [35], we compute solutions to the model using the following stages. To do so, we must have a priori knowledge of the  $Q$ -factor of the structure, either from a laboratory experiment or, for the results in this paper, from simulations obtained using the two-way coupled model.

1. Determine the physically relevant eigenfrequency,  $\omega_0$ , of the undamped structure, as described in the supplementary material (suppmats.pdf [local/web 228KB]).
2. Fit the ad hoc damping parameter,  $\delta_S$ , so that for  $\omega$  near  $\omega_0$  the resonance curve computed using (2.9) gives the desired  $Q$ -factor of the structure via (1.1). Then choose the resonant driving frequency,  $\omega_{\text{res}}$ , to be at the maximum of the resonance curve.
3. Using the value of  $\omega_{\text{res}}$  obtained in stage 2, solve the pressure-temperature subsystem of the Morse–Ingard equations in the fluid coupled to the heat equation in the structure via the interface conditions (2.4), (2.6), and (2.7).
4. Using the values of  $\delta_S$  and  $\omega_{\text{res}}$  from stage 2 and the pressure-temperature solution from stage 3, compute the deformation of the structure using the equation of linear elasticity given in (2.9) and the interface condition (2.10).

We note that for a spring-mass system,

$$(2.11) \quad m \frac{d^2 u}{dt^2} + b \frac{du}{dt} + ku = F_0 \cos(\omega t),$$

the damping parameter,  $b$ , is related to the  $Q$ -factor by the equation  $b/m = \omega_0/Q$  [4, p. 83]. However, for the one-way coupled model it is not possible to derive a similar formula relating the damping parameter,  $\delta_S$ , to the  $Q$ -factor.

**2.2. Two-way coupled model.** With the one-way coupled models of Petra et al. [34], Firebaugh and colleagues [14, 15], and Safin, Zweck, and Minkoff [39], damping is incorporated in an ad hoc manner that requires a priori knowledge of the  $Q$ -factor of the tuning fork. When using these models, the  $Q$ -factor is obtained by making laboratory measurements with particular tuning forks. Consequently, these models cannot be used with arbitrary QTF geometries. On the other hand, with the two-way coupled model, viscous damping is incorporated through the viscosity parameters in (2.2) and, more importantly, via interface conditions on the fluid due to the structure and on the structure due to the fluid. Consequently, with the two-way coupled model the  $Q$ -factor is an output of the model rather than being an input parameter. Therefore the two-way coupled model allows for the modeling of arbitrary structural geometries and hence can be used to numerically optimize the geometric configuration of the tuning fork in a QEPAS or ROTADE sensor. The disadvantage of the two-way coupled model is that all the equations in the model must be solved simultaneously with the interface and boundary conditions, whereas with the one-way coupled model we first solve the fluid system and then the structural system.

In the two-way coupled model, the conditions on the fluid-structure interface involve the fluid velocity,  $\mathbf{v}$ , which satisfies the Helmholtz form of the linearized Navier–Stokes equations [30]

$$(2.12) \quad -i\omega\rho_F \mathbf{v} = -\nabla p + (\eta_F + \frac{4}{3}\mu_F) \nabla(\nabla \cdot \mathbf{v}) - \mu_F \nabla \times (\nabla \times \mathbf{v}).$$

We impose the following conditions for  $p$ ,  $\tau_F$ ,  $\mathbf{v}$ ,  $\tau_S$ , and  $\mathbf{u}$  on the fluid-structure interface. For the interface condition on the fluid velocity, we suppose that the fluid does not penetrate into the structure and that a no-slip condition holds, which is reasonable, since the fluid is slightly viscous. With time harmonic forcing, these assumptions imply that

$$(2.13) \quad \mathbf{v} = -i\omega \mathbf{u} \quad \text{on } \partial\Omega_{FS}.$$

To obtain the interface condition on the structural displacement due to the fluid, we use Newton's third law, which states that

$$(2.14) \quad \boldsymbol{\sigma}_S \mathbf{n} = \boldsymbol{\sigma}_F^{\text{Tot}} \mathbf{n} \quad \text{on } \partial\Omega_{FS}.$$

The total fluid stress tensor on the right-hand side of (2.14) is given by  $\boldsymbol{\sigma}_F^{\text{Tot}} = -p\mathbf{I} + \boldsymbol{\sigma}_F$ , where the viscous stress tensor,

$$(2.15) \quad (\boldsymbol{\sigma}_F)_{jk} = \mu_F \left( \frac{\partial v_j}{\partial x_k} + \frac{\partial v_k}{\partial x_j} - \frac{2}{3} \delta_{jk} \nabla \cdot \mathbf{v} \right) + \eta_F \delta_{jk} \nabla \cdot \mathbf{v},$$

models the frictional force acting on the structure due to the viscous fluid [25, sect. 15]. Therefore by (2.8), on the free portion, the interface condition on the structural displacement due to the fluid (2.14) is given by

$$(2.16) \quad (\mathbf{C}[\nabla \mathbf{u}] - \mathbf{C}[\boldsymbol{\alpha}_S \tau_S]) \mathbf{n} = -p \mathbf{n} + \boldsymbol{\sigma}_F \mathbf{n} \quad \text{on } \partial\Omega_S^{\text{Free}}.$$

On the fixed portion,  $\partial\Omega_S^{\text{Fixed}}$ , of the boundary of the structure, we instead impose the conditions  $\mathbf{u} = \mathbf{0}$  and  $\nabla \mathbf{u} = \mathbf{0}$ .

To calculate the resonance frequency, we solve the two-way coupled model for a range of driving frequencies,  $\omega$ , near  $\omega_0$  and set  $\omega_{\text{res}}$  to be the frequency that gives the maximum of the resulting resonance curve. The signal strength is then chosen to be that computed at  $\omega = \omega_{\text{res}}$ .

To summarize, the PDEs for the one-way coupled model are

$$(2.17) \quad \Omega \Delta \tau_F + i \left( \frac{\omega}{c} \right)^2 \left( \tau_F - \frac{\gamma-1}{\gamma \alpha} p \right) = -\frac{\omega}{c^2} S \quad \text{in } \Omega_F,$$

$$(2.18) \quad \Delta p + \frac{\gamma}{c^2} (\omega^2 - i c^2 \Lambda \Delta) (p - \alpha \tau_F) = 0 \quad \text{in } \Omega_F,$$

$$(2.19) \quad i \omega \tau_S + D_S \Delta \tau_S = 0 \quad \text{in } \Omega_S,$$

$$(2.20) \quad \nabla \cdot \mathbf{C}[\nabla \mathbf{u}] + (\rho_S \omega^2 - i \omega \delta_S) \mathbf{u} = \nabla \cdot \mathbf{C}[\boldsymbol{\alpha}_S \tau_S] \quad \text{in } \Omega_S.$$

For the two-way coupled model, we also include the linearized Navier–Stokes equation (2.12), and we set  $\delta_S = 0$  in (2.20). For the one-way coupled model, the interface conditions are

$$(2.21) \quad \tau_S = \tau_F \quad \text{on } \partial\Omega_{FS},$$

$$(2.22) \quad K_S \nabla \tau_S \cdot \mathbf{n} = K_F \nabla \tau_F \cdot \mathbf{n} \quad \text{on } \partial\Omega_{FS},$$

$$(2.23) \quad \nabla p \cdot \mathbf{n} = 0 \quad \text{on } \partial\Omega_{FS},$$

$$(2.24) \quad (\mathbf{C}[\nabla \mathbf{u}] - \mathbf{C}[\boldsymbol{\alpha}_S \tau_S]) \mathbf{n} = -p \mathbf{n} \quad \text{on } \partial\Omega_S^{\text{Free}},$$

$$(2.25) \quad \mathbf{u} = \mathbf{0} \quad \text{and} \quad \nabla \mathbf{u} = \mathbf{0} \quad \text{on } \partial\Omega_S^{\text{Fixed}},$$

while for the two-way coupled model, we use (2.21), (2.22), and (2.25) together with

$$(2.26) \quad (1 - i\gamma\Lambda)\nabla p \cdot \mathbf{n} + i\alpha\gamma\Lambda\nabla\tau_F \cdot \mathbf{n} = \rho_F\omega^2\mathbf{u} \cdot \mathbf{n} \quad \text{on } \partial\Omega_S^{\text{Free}},$$

$$(2.27) \quad (\mathbf{C}[\nabla\mathbf{u}] - \mathbf{C}[\boldsymbol{\alpha}_S\tau_S])\mathbf{n} = -p\mathbf{n} + \boldsymbol{\sigma}_F\mathbf{n} \quad \text{on } \partial\Omega_S^{\text{Free}},$$

$$(2.28) \quad \mathbf{v} = -i\omega\mathbf{u} \quad \text{on } \partial\Omega_{FS}.$$

The interface conditions in the two-way coupled model are consistent with those given by Joly, Bruneau, and Bossart [17] in their model for linear acoustics in a thermo-viscous fluid.

**3. Analytic solution in a special case with cylindrical symmetry.** In this section, we derive analytic solutions for the one-way and two-way coupled models in a special case in which the fluid and structural domains are cylindrically symmetric. In this case, the Helmholtz PDE systems in section 2 reduce to systems of Bessel equations in the radial variable. In subsection 3.1 we describe the cylindrically symmetric geometry and alternate formulations of the equation and interface condition for the fluid velocity. In subsection 3.2, we review the general solution of the pressure and temperature subsystem obtained by Kaderli et al. [18]. In subsection 3.3, we derive the general solution of the linear elastic equations in the structure. Finally, in subsection 3.4, we use the interface and boundary conditions for each model to formulate a  $6 \times 6$  linear system for the unknown coefficients in these general solutions.

**3.1. Cylindrically symmetric geometry.** To facilitate the derivation of an analytical solution to the Helmholtz system of PDEs discussed in subsection 2.2, we consider the special case in which the fluid domain,  $\Omega_F$ , is an infinite solid cylinder of radius  $R_1$ , and the structural domain,  $\Omega_S$ , is an infinite cylindrical tube surrounding  $\Omega_F$  with inner radius  $R_1$  and outer radius  $R_2$  (see Figure 1). We let  $r$  denote the radial distance from the axis of the cylinder. Because we have assumed that the source is  $z$ -independent, the problem can be formulated on a two-dimensional slice. Indeed, all scalar fields are functions of  $r$  only, while the vector fields are of the form  $\mathbf{v}(r, \theta) = v(r)\mathbf{e}_r(r, \theta)$ , where  $\mathbf{e}_r$  is the unit vector in the radial direction at  $(r, \theta)$ .

With this geometry, the linearized Navier–Stokes equation (2.12) and the interface condition (2.13) on the fluid velocity can be reformulated to facilitate the solution of the model. To do so, we use the Helmholtz decomposition theorem [9], to uniquely express the fluid velocity in a general domain,  $\Omega_F$ , as  $\mathbf{v} = \mathbf{v}_\ell + \mathbf{v}_t$ , where the lamellar or longitudinal part,  $\mathbf{v}_\ell$ , of  $\mathbf{v}$  is curl free, and the rotational or transverse part,  $\mathbf{v}_t$ , is divergence free and tangent to the boundary,  $\partial\Omega_F$ . Then (2.12) is equivalent to the pair of equations<sup>3</sup> [30]

$$(3.1) \quad -i\omega\rho_F\mathbf{v}_\ell = -\nabla[(1 - i\gamma\Lambda)p + i\alpha\gamma\Lambda\tau_F],$$

$$(3.2) \quad -i\omega\rho_F\mathbf{v}_t = -\mu_F\nabla \times (\nabla \times \mathbf{v}_t).$$

Furthermore, by (3.1) the interface condition (2.13) for  $\mathbf{v}$  implies that for general domains,

$$(3.3) \quad (1 - i\gamma\Lambda)\nabla p \cdot \mathbf{n} + i\alpha\gamma\Lambda\nabla\tau_F \cdot \mathbf{n} = \rho_F\omega^2\mathbf{u} \cdot \mathbf{n} \quad \text{on } \partial\Omega_F.$$

In the special case that the fluid domain,  $\Omega_F$ , is a disc, the Helmholtz decomposition theorem implies that  $\mathbf{v}_t = 0$  and  $\mathbf{v}_\ell = \mathbf{v}$ . Therefore, the linearized Navier–Stokes

---

<sup>3</sup>With this alternative formulation of (2.12), (2.1) and (2.2) form a coupled subsystem for  $p$  and  $\tau_F$ , while (3.1) enables  $\mathbf{v}_\ell$  to be computed from  $p$  and  $\tau_F$ . Although  $\mathbf{v}_t$  appears to be independent of the other variables, in practice it is coupled to  $p$ ,  $\tau_F$ , and  $\mathbf{v}_\ell$  via boundary and interface conditions.

equation (2.12) is equivalent to (3.1). In addition, since  $\mathbf{u}_t = 0$  and  $\mathbf{u}_\ell = \mathbf{u}$  in the annular structure,  $\Omega_S$ , the interface condition (3.3) is actually equivalent to the interface condition (2.13) for the fluid velocity, not just a consequence of it. However, for general geometries, (2.13) is not guaranteed to hold if (3.3) does, since  $\mathbf{v}_t \neq \mathbf{0}$  and  $\mathbf{v}_\ell$  may have a component that is tangent to the boundary.

**3.2. The fluid equations.** In the cylindrically symmetric setting the one-way and two-way coupled models both reduce to a system of ODEs with boundary and interface conditions. Since  $\nabla = \partial_r \mathbf{e}_r$  in polar coordinates, equations (2.1), (2.2), and (3.1), for the temperature, pressure, and the velocity of the fluid, reduce to the ODE system

$$(3.4) \quad \frac{\Omega c^2}{\omega} \Delta \tau_F + i\omega \left( \tau_F - \frac{\gamma-1}{\gamma\alpha} p \right) = -S,$$

$$(3.5) \quad \Delta p + \frac{\gamma}{c^2} (\omega^2 - i c^2 \Lambda \Delta) (p - \alpha \tau_F) = 0,$$

$$(3.6) \quad v = \left( \frac{1}{i \rho_F \omega} - \frac{\gamma \Lambda}{\rho_F \omega} \right) p' + \frac{\alpha \gamma \Lambda}{\rho_F \omega} \tau'_F,$$

where  $\Delta = \partial_r^2 + \frac{1}{r} \partial_r$  is the radial Laplacian operator on  $\mathbb{R}^2$  and  $' = \partial_r$ .

Kaderli et al. [18] used the method of variation of parameters to derive an analytic solution of (3.4) and (3.5), which is given in terms of the nondimensional quantities

$$\begin{aligned} \tilde{r} &= \frac{r}{r_c}, & \tilde{\Delta} &= \frac{\Delta}{r_c^2}, & \tilde{p} &= \frac{p}{p_0}, \\ \tilde{\tau}_F &= \frac{\alpha}{p_0} \tau_F, & \tilde{\mathbf{v}} &= \frac{\mathbf{v}}{v_c}, & \tilde{S} &= -\frac{\alpha}{\omega} S, \end{aligned}$$

where  $r_c = \frac{c}{\omega}$ ,  $v_c = 1$ , and  $p_0 = 1$ . Substituting these quantities into (3.4) and (3.5), the equations become

$$(3.7) \quad \tilde{\Delta} \tilde{p} + \gamma (1 - i \Lambda \tilde{\Delta}) (\tilde{p} - \tilde{\tau}_F) = 0,$$

$$(3.8) \quad \Omega \tilde{\Delta} \tilde{\tau}_F + i \left( \tilde{\tau}_F - \frac{\gamma-1}{\gamma} \tilde{p} \right) = \tilde{S}.$$

Following Morse and Ingard [30, p. 284], we introduce the temperature and pressure mode constants,  $\kappa_t$  and  $\kappa_p$ , which are given by

$$\kappa_t^2 = \frac{i}{2\Omega} \left( \frac{1 - i\gamma\Omega - i\Lambda + Q}{1 - i\gamma\Lambda} \right), \quad \kappa_p^2 = \frac{i}{2\Omega} \left( \frac{1 - i\gamma\Omega - i\Lambda - Q}{1 - i\gamma\Lambda} \right),$$

where  $Q^2 = (1 - i\gamma\Omega - i\Lambda)^2 + 4(i\Omega + \gamma\Omega\Lambda)$ . Kaderli et al. [18] showed that the general solution of (3.7) and (3.8) can be expressed as

$$(3.9) \quad \begin{aligned} \tilde{p}(\tilde{r}) &= m_p \left[ (b_1 + c_1(\tilde{r})) J_0(\kappa_p \tilde{r}) + c_2(\tilde{r}) H_0^{(1)}(\kappa_p \tilde{r}) \right] \\ &\quad + m_t \left[ (b_2 + c_3(\tilde{r})) J_0(\kappa_t \tilde{r}) + c_4(\tilde{r}) H_0^{(1)}(\kappa_t \tilde{r}) \right], \end{aligned}$$

$$(3.10) \quad \begin{aligned} \tilde{\tau}_F(\tilde{r}) &= (b_1 + c_1(\tilde{r})) J_0(\kappa_p \tilde{r}) + c_2(\tilde{r}) H_0^{(1)}(\kappa_p \tilde{r}) \\ &\quad + (b_2 + c_3(\tilde{r})) J_0(\kappa_t \tilde{r}) + c_4(\tilde{r}) H_0^{(1)}(\kappa_t \tilde{r}), \end{aligned}$$

where  $J_0$  and  $H_0^{(1)}$  are the Bessel and Hankel functions of the first kind. Here  $b_1$  and  $b_2$  are arbitrary constants, and the constants  $m_p$  and  $m_t$  are given by

$$(3.11) \quad m_t = \frac{\gamma}{\gamma - 1} (1 + i\Omega \kappa_t^2), \quad m_p = \frac{\gamma}{\gamma - 1} (1 + i\Omega \kappa_p^2).$$

The functions  $c_j$  are overlap integrals of the basis functions with the source (see [18]). Finally, the fluid velocity,  $\tilde{v}$ , can be expressed in terms of the derivatives of  $\tilde{p}$  and  $\tilde{\tau}_F$  using (3.6). We observe that the pressure and temperature in (3.9) and (3.10) are both expressed as the sum of a propagational mode and a thermal mode which are given by the terms involving the constants  $\kappa_p$  and  $\kappa_t$ , respectively. Because  $\Omega$  and  $\Lambda$  are typically on the order of  $10^{-5}$ , the phases of  $\kappa_p$  and  $\kappa_t$  are small positive numbers. Consequently, the thermal mode is a rapidly decaying function of  $r$  and the propagation mode decays much more slowly.

Similarly, the solution of the Helmholtz form of the heat equation in the structure (2.5) is given by

$$(3.12) \quad \tilde{\tau}_S(\tilde{r}) = b_3 J_0(\lambda \tilde{r}) + b_4 H_0^{(1)}(\lambda \tilde{r}),$$

where  $\lambda = e^{i\pi/4} \left( \frac{\omega r_s^2}{D_S} \right)^{\frac{1}{2}}$  and  $b_3, b_4$  are arbitrary constants to be determined by the interface and boundary conditions.

**3.3. The structural equations.** We now determine the analytic solution of the elastic deformation equation (2.9) for the structure, which was not discussed in Kaderli et al. [18].

We suppose for simplicity that the structure is an isotropic, homogeneous elastic medium, in which case the stress and strain tensors are related by [8, p. 317]

$$(3.13) \quad \mathbf{C}[\boldsymbol{\epsilon}_S] = \lambda_S \text{Tr}(\boldsymbol{\epsilon}_S) \mathbf{I} + 2\mu_S \boldsymbol{\epsilon}_S.$$

With radial symmetry, the displacement of the structure is of the form  $\mathbf{u}(r, \theta) = u(r) \mathbf{e}_r(\theta)$ , where  $\mathbf{e}_r$  is the unit vector in the radial direction. Applying the formula for the strain tensor in cylindrical coordinates [40, p. 11] and using (3.13), we find that the Helmholtz form of the equation for the time periodic displacement of the structure (2.9) reduces to the inhomogeneous Bessel equation

$$(3.14) \quad (\lambda_S + 2\mu_S) \left( u'' + \frac{1}{r} u' - \frac{1}{r^2} u \right) + \rho_S \omega^2 u = \zeta_1 \tau'_S,$$

where  $\zeta_1 = \alpha_S(3\lambda_S + 2\mu_S)$ . We nondimensionalize (3.14) using the dimensionless quantities  $\tilde{u} = u/u_c$  and  $\tilde{r} = r/r_s$ , where

$$(3.15) \quad u_c = \frac{p_0 r_s \zeta_1}{\alpha(\lambda_S + 2\mu_S)} \quad \text{and} \quad r_s = \sqrt{\frac{\lambda_S + 2\mu_S}{\rho_S \omega^2}}.$$

Substituting these quantities into (3.14) gives the nondimensionalized equation,

$$(3.16) \quad \tilde{u}'' + \frac{1}{\tilde{r}} \tilde{u}' + \left( \kappa_u^2 - \frac{1}{\tilde{r}^2} \right) \tilde{u} = \tilde{\tau}'_S,$$

where  $\kappa_u^2 = \frac{\rho_S \omega^2 r_s^2}{\lambda_S + 2\mu_S}$ . Therefore, the general solution of (3.16) can be expressed in terms of the Bessel functions  $J_1$  and  $Y_1$  as

$$(3.17) \quad \begin{aligned} \tilde{u}(\tilde{r}) = & b_5 J_1(\kappa_u \tilde{r}) + b_6 Y_1(\kappa_u \tilde{r}) - \frac{\pi}{2} J_1(\kappa_u \tilde{r}) \int_{\tilde{R}_{1S}}^{\tilde{r}} s Y_1(\kappa_u s) \tilde{\tau}'_S(s) ds \\ & + \frac{\pi}{2} Y_1(\kappa_u \tilde{r}) \int_{\tilde{R}_{1S}}^{\tilde{r}} s J_1(\kappa_u s) \tilde{\tau}'_S(s) ds, \end{aligned}$$

where  $b_5$  and  $b_6$  are arbitrary constants,  $\tilde{R}_{1S} = R_1/r_s$  and  $\tilde{\tau}_S$  is given by (3.12).

**3.4. Interface and boundary conditions.** In the previous subsections we derived formulae for the general solutions of the PDEs in the one-way and two-way coupled models in terms of Bessel and Hankel functions. These formulae are given in terms of six unknown constants  $b_1, \dots, b_6$ . To determine these constants we use the interface and the boundary conditions to obtain a system of six linear equations,  $\mathbf{Ab} = \mathbf{F}$ . For the two-way model this system is of the form

$$(3.18) \quad \begin{bmatrix} a_{11} & a_{12} & a_{13} & a_{14} & 0 & 0 \\ 0 & 0 & a_{23} & a_{24} & 0 & 0 \\ a_{31} & a_{32} & a_{33} & a_{34} & 0 & 0 \\ 0 & 0 & a_{43} & a_{44} & a_{45} & a_{46} \\ a_{51} & a_{52} & 0 & 0 & a_{55} & a_{56} \\ a_{61} & a_{62} & a_{63} & a_{64} & a_{65} & a_{66} \end{bmatrix} \begin{bmatrix} b_1 \\ b_2 \\ b_3 \\ b_4 \\ b_5 \\ b_6 \end{bmatrix} = \begin{bmatrix} F_1 \\ F_2 \\ F_3 \\ F_4 \\ F_5 \\ F_6 \end{bmatrix}.$$

Formulae for the entries  $a_{ij}$  and  $F_i$  can be found in the supplementary material (suppmats.pdf [local/web 228KB]). In particular, we use the interface condition (3.3) for the pressure rather than the equivalent condition (2.13) on the fluid velocity.

For the one-way coupled model,  $\mathbf{A}$  has two additional zero entries, namely  $a_{55} = 0$  and  $a_{56} = 0$ . In addition, the first four rows of  $\mathbf{A}$  and  $\mathbf{F}$  are the same as for the two-way coupled model except that the parameter  $\kappa_u$  is modified to account for the heuristically added damping term in the structural displacement equation, namely,

$$\kappa_u^2 = \frac{(\rho_S \omega^2 - i \omega \delta_S) r_s^2}{\lambda_S + 2\mu_S}.$$

**4. Numerical results.** In this section, we use the analytic solution for the annular geometry derived in section 3 to compare the results obtained from the two-way coupled model with those from the one-way model when we vary the ambient pressure. For the two-way coupled model, we also show agreement with results obtained from a finite element implementation, which provides confidence in the correctness of both solution methods.<sup>4</sup> The main insights obtained from these results are as follows.

1. At higher ambient pressures there is a lack of quantitative agreement between the one-way and two-way coupled models. This discrepancy occurs because damping is implemented differently in the two models, which results in differently shaped resonance curves.
2. The  $Q$ -factor computed using the two-way coupled model increases as the ambient pressure decreases. This finding is consistent with experimental results for trace gas sensors.
3. However, for the annular geometry the larger  $Q$ -factor does not result in a larger signal strength. Instead, with the two-way coupled model there is a gradual decrease in the signal strength since the average acoustic pressure is proportional to the ambient pressure.

---

<sup>4</sup>The finite element formulation of the two-way model is described in the appendix.

TABLE 1  
*Parameters used in the numerical simulations.*

Parameter list	
Name	Value
Ambient temperature	$T_0 = 293.15\text{K}$
Ambient pressure	$P_0$ varies from 5 Torr to 450 Torr
Specific gas constant for nitrogen	$R_0 = 296.80 \text{ J kg}^{-1} \text{ K}^{-1}$
Inner radius of the annulus	$R_1 = 100 \mu\text{m}$
Outer radius of the annulus	$R_2 = 200 \mu\text{m}$
Source width	$\sigma = 20 \mu\text{m}$
Density of nitrogen gas	$\rho_F = P_0/(R_0 T_0) \text{ kg m}^{-3}$
Density of quartz	$\rho_S = 2650 \text{ kg m}^{-3}$
Thermal expansion coefficient of quartz	$\alpha_S = 13.7 \times 10^{-6} \text{ K}^{-1}$
Viscosity of the nitrogen gas	$\mu_F = 1.79 \times 10^{-5} \text{ kg m}^{-1} \text{ s}^{-1}$
Bulk viscosity of the nitrogen gas	$\eta_F = 1.32 \times 10^{-5} \text{ kg m}^{-1} \text{ s}^{-1}$
Thermal conductivity of nitrogen gas	$K_F = 0.0254 \text{ W m}^{-1} \text{ K}^{-1}$
Specific heat capacity of nitrogen gas	$C_p = 1040 \text{ J kg}^{-1} \text{ K}^{-1}$
Thermal conductivity of quartz	$K_S = 6.5 \text{ W m}^{-1} \text{ K}^{-1}$
Specific heat capacity of quartz	$C_{pS} = 733 \text{ J kg}^{-1} \text{ K}^{-1}$
Thermal diffusivity of quartz	$D_S = K_S/(\rho_S C_{pQ}) \text{ m}^2 \text{ s}^{-1}$
Thermal diffusivity of nitrogen gas	$D_F = K_F/(\rho_F C_p) \text{ m}^2 \text{ s}^{-1}$
Ratio of specific heats of nitrogen gas	$\gamma = 1.4$
Thermal expansion of nitrogen gas	$\beta = 1/T_0 \text{ K}^{-1}$
Speed of sound in nitrogen gas	$c = \sqrt{\gamma P_0/\rho_F} \text{ m/s}$
Effective absorption coefficient	$\alpha_{\text{eff,ref}} = 10^{-3} \text{ m}^{-1}$ at $P_{\text{ref}} = 50 \text{ Torr}$
Laser power	$W_L = 0.03 \text{ W}$
Characteristic length of heat conductivity	$\ell_h = K_F/(\rho_F c C_p) \text{ m}$
Characteristic length of viscosity	$\ell_v = (\eta_F + \frac{4}{3}\mu_F)/(\rho_F c) \text{ m}$
$\frac{\partial p}{\partial \tau}$ under constant volume	$\alpha = P_0/T_0 \text{ Pa K}^{-1}$
Lamé parameter	$\lambda_S = 2 \times 10^5 \text{ N m}^{-2}$
Lamé parameter	$\mu_S = 1 \times 10^5 \text{ N m}^{-2}$

- At low ambient pressure (less than 50 Torr), the one-way model considerably overestimates the signal strength compared to the two-way model.
- The fluid velocity, which is determined by a combination of the gradients of acoustic pressure and temperature, behaves quite differently for the two models.
- With the two-way model, as the ambient pressure decreases, the thermal component of the fluid velocity plays a more prominent role in the interface condition relating the fluid velocity to the structural displacement. The reason for the considerable disagreement between the two models at low ambient pressure is that this effect is not captured by the one-way model.

The parameter values we used in the numerical simulations are shown in Table 1. The source parameters and physical constants were chosen to be the same as for an experimental QEPAS or ROTADE sensor, except that we artificially changed the values of the Lamé parameters,  $\lambda_S$  and  $\mu_S$ , so that the undamped resonance frequency of the annulus was 33.5 kHz, which is on the same order as the 32.8 kHz resonance frequency of a standard QTF [21].

We begin by plotting the resonance curves for several values of the ambient pressure. In a trace gas sensor, the measured electric current is proportional to the

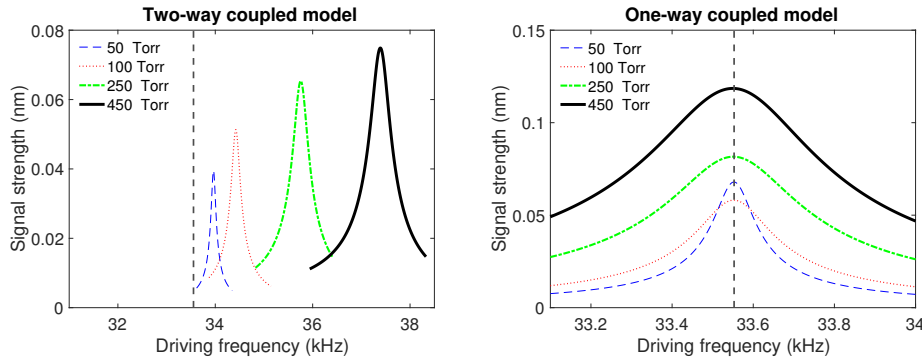


FIG. 2. Resonance curves for several values of the ambient pressure. Left: Two-way coupled model. Right: One-way coupled model.

displacement of the tuning fork at the tip of a tine [21]. For the annulus, the analogous quantity to consider is the displacement at the inner surface of the vibrating structure. Henceforth, we refer to this quantity as the signal strength. In Figure 2 (left), we plot the signal strength as a function of driving frequency,  $\omega$ , for the two-way coupled model at ambient pressures of 50, 100, 250, and 450 Torr.<sup>5</sup> We observe that these resonance curves are slightly asymmetric and that as the ambient pressure decreases, the signal strength decreases and the resonance frequency decreases towards the undamped resonance frequency of 33.5 kHz. In Figure 2 (right), we plot the corresponding results for the one-way coupled model. In contrast to the results for the two-way model, for this model the peaks of the resonance curves agree almost exactly with the undamped resonance frequency. Further, the signal strength decreases as the ambient pressure decreases until the ambient pressure falls below about 100 Torr. Then, anomalously, it starts to increase. This last observation is corroborated by the results in Table 2. In this table, for ambient pressures ranging from 450 Torr down to 5 Torr, we show the  $Q$ -factor (column 2) as a function of the ambient pressure (column 1). The rapid increase in the  $Q$ -factor as the ambient pressure decreases is consistent with previously reported experimental and theoretical studies in cantilevers and tuning forks [1, 2]. We recall that the input damping parameter,  $\delta_S$ , in the one-way model (column 3) is chosen so that the width of the resonance curves is the same as for the two-way model (column 5), and that the  $Q$ -factor is obtained from the width using (1.1). Finally, we show the maximum signal strength for the one-way model (column 4) and the two-way model (column 6). In Figure 3, we plot the maximum signal strength as a function of ambient pressure. For both models down to 100 Torr we see a gradual decrease in the signal strength. For the two-way model this trend continues down to 5 Torr, but for the one-way model the signal strength increases dramatically. Significantly, we observe that even though the  $Q$ -factor increases as ambient pressure decreases, at least for the two-way model, the signal strength does not increase. To understand these trends, we next examine the behavior of the fluid variables.

In Table 3, we show the average of the pressure variation,  $p$ , in the fluid as a function of ambient pressure,  $P_0$ , for the two models. We note that the function  $p = p(r)$  is approximately constant since  $1/\kappa_p$  is large compared to the inner radius of the annulus, where  $\kappa_p$  is the parameter in (3.9). For the one-way model,

<sup>5</sup>Atmospheric pressure is 760 Torr.

TABLE 2

*Input damping parameter  $\delta_S$  (column 3) for the one-way coupled model obtained from the width of the resonance curve for the two-way coupled model (column 5) as a function of ambient pressure (column 1). We also show the maximum signal strength for both models (columns 4 and 6) and the Q-factor (column 2).*

$P_0$ (Torr)	$Q$ -factor	One-way coupled model		Two-way coupled model	
		$\delta_s$	Signal (nm)	Width (Hz)	Signal (nm)
450	94	$6.63 \times 10^6$	0.1185	398.7	0.0749
250	114	$5.2 \times 10^6$	0.0816	312.4	0.0654
100	188	$3.05 \times 10^6$	0.0581	183.0	0.0513
50	345	$1.64 \times 10^6$	0.0679	98.5	0.0395
20	1361	$4.123 \times 10^5$	0.1410	24.8	0.0330
15	2309	$2.428 \times 10^5$	0.1870	14.6	0.0325
10	5072	$1.104 \times 10^5$	0.2840	6.6	0.0326
5	21671	$2.58 \times 10^4$	0.6200	1.6	0.0354

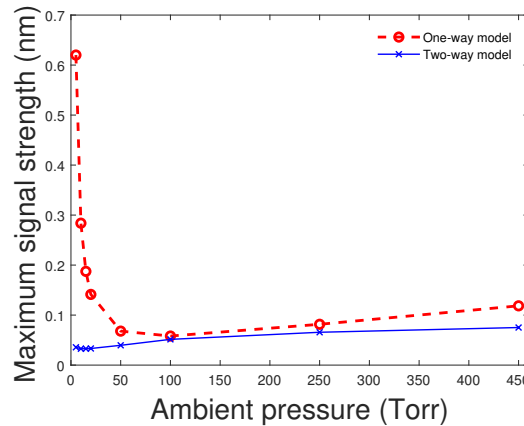


FIG. 3. Maximum signal strength for both models as a function of ambient pressure.

TABLE 3

*The average fluid pressure for both models tabulated as a function of ambient pressure.*

Ambient pressure	Pressure variation (kPa)		
	5 Torr	50 Torr	450 Torr
One-way coupled model	$1.7 \times 10^{-7}$	$1.2 \times 10^{-6}$	$8.4 \times 10^{-6}$
Two-way coupled model	$4.6 \times 10^{-7}$	$5.9 \times 10^{-6}$	$1.2 \times 10^{-4}$

$p$  is proportional to  $P_0$ , since to first order  $p$  satisfies the acoustic wave equation with a zero Neumann boundary condition and a source that is proportional to  $P_0$ . On the other hand, for the two-way model,  $p$  increases more rapidly due to the  $P_0$ -dependence of the coefficient on the right-hand side of the interface condition (3.3) for the pressure and temperature. As we see in Figures 4–6, the maximum values of the fluid temperature and velocity also decrease as  $P_0$  decreases. These trends, which are due to the linearity of the equations, result in a similar decrease in the signal strength (except for the one-way model below 100 Torr). In summary, the gradual decrease in the signal strength shown in Figure 3 is primarily due to the decrease in the average acoustic pressure. On the other hand, we will argue below that

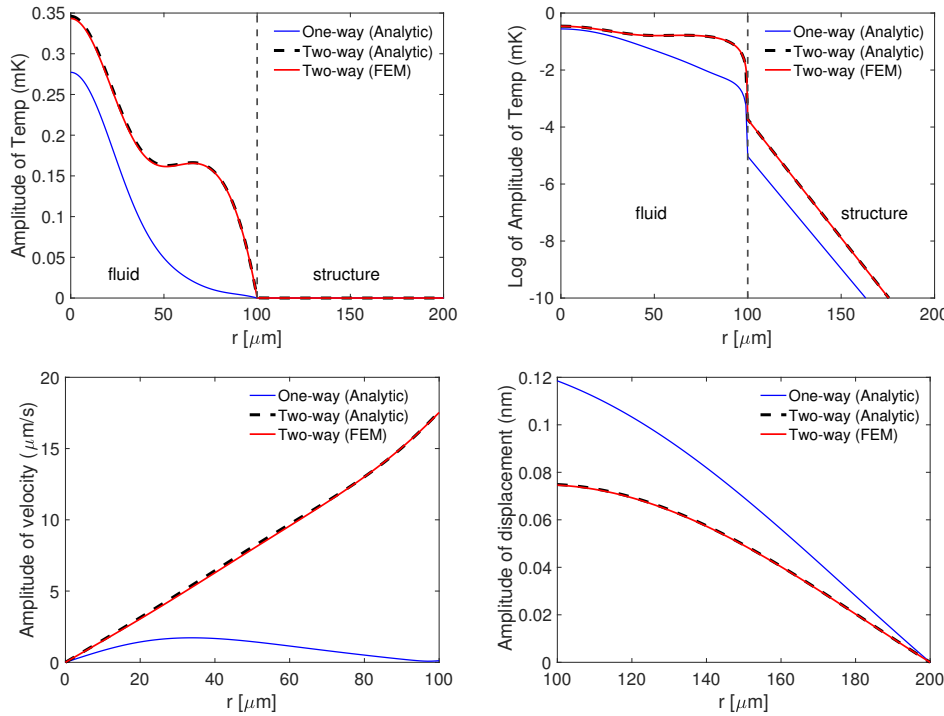


FIG. 4. Comparison of the results obtained with the one-way and two-way coupled models at an atmospheric pressure of 450 Torr. We show the temperature variation on a linear scale (top left) and on a logarithmic scale (top right), the amplitude of the fluid velocity (bottom left), and the amplitude of the displacement of the structure (bottom right). These quantities are plotted as functions of the radial distance ( $r$ ) from the center of the laser beam. We show results obtained using the analytic solution of the one-way model (solid blue line), the analytic solution of the two-way model (dashed black line), and the finite element solution (solid red line) from the two-way model. (Color figure available online.)

with the one-way model, as the ambient pressure decreases below 50 Torr, the signal strength increases rapidly because this simplified model does not adequately capture the damping processes at low ambient pressure.

In Figure 4, we plot the amplitude of the temperature as a function of radial distance,  $r$ , on a linear scale (top left) and a logarithmic scale (top right) at an ambient pressure of  $P_0 = 450$  Torr. For each model, the laser frequency is chosen to equal the resonance frequency obtained from the results in Figure 2. The fluid-structure interface at  $r = 100 \mu\text{m}$  is shown with the vertical dashed line. Examining the linear-scale temperature plot, for the two-way model, we see the influence of the Gaussian source term in the region  $r < 40 \mu\text{m}$ . The ledge evident in the region  $r \in [40, 80] \mu\text{m}$  is due to the influence of the pressure, which is approximately constant and which dominates over the source term in this region. In the top rows of Figures 5 and 6 we observe similar trends at ambient pressures of 50 Torr and 5 Torr, respectively, although they are not as pronounced. Finally, we observe in the top right panel of Figure 4 that at 450 Torr the temperature at the interface is about 1.5 orders of magnitude smaller with the one-way model than with the two-way model, since as we see in Table 3, the average pressure is 15 times smaller.

In the bottom row of Figure 4 we plot the amplitude of the fluid velocity (left) and the amplitude of the structural displacement (right) at an ambient pressure of

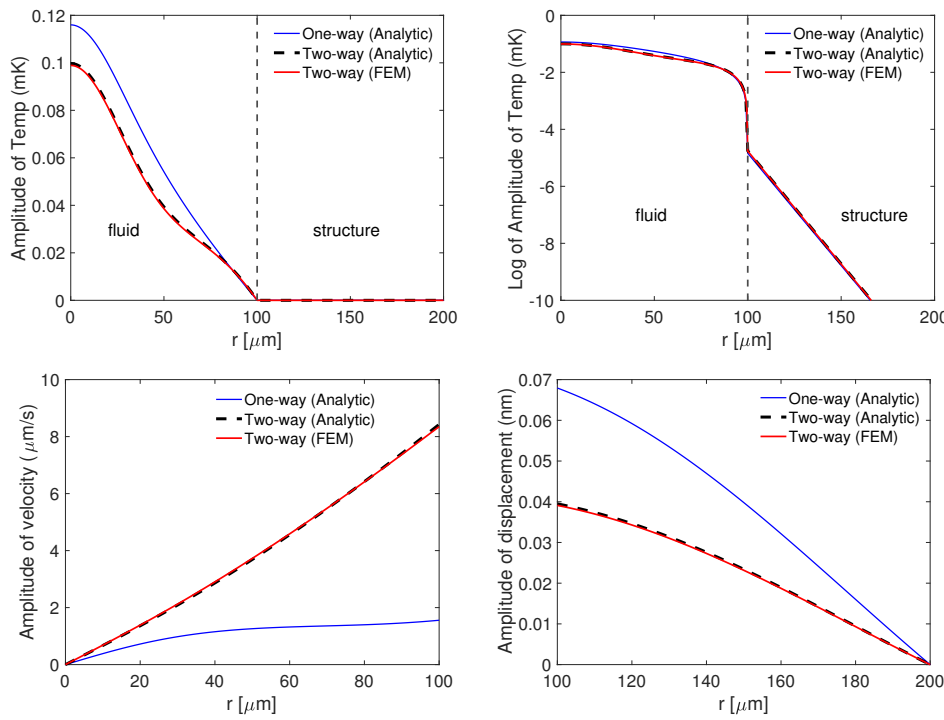


FIG. 5. Comparison of the results obtained with the one-way and two-way coupled models at an atmospheric pressure of 50 Torr. (Color figure available online.)

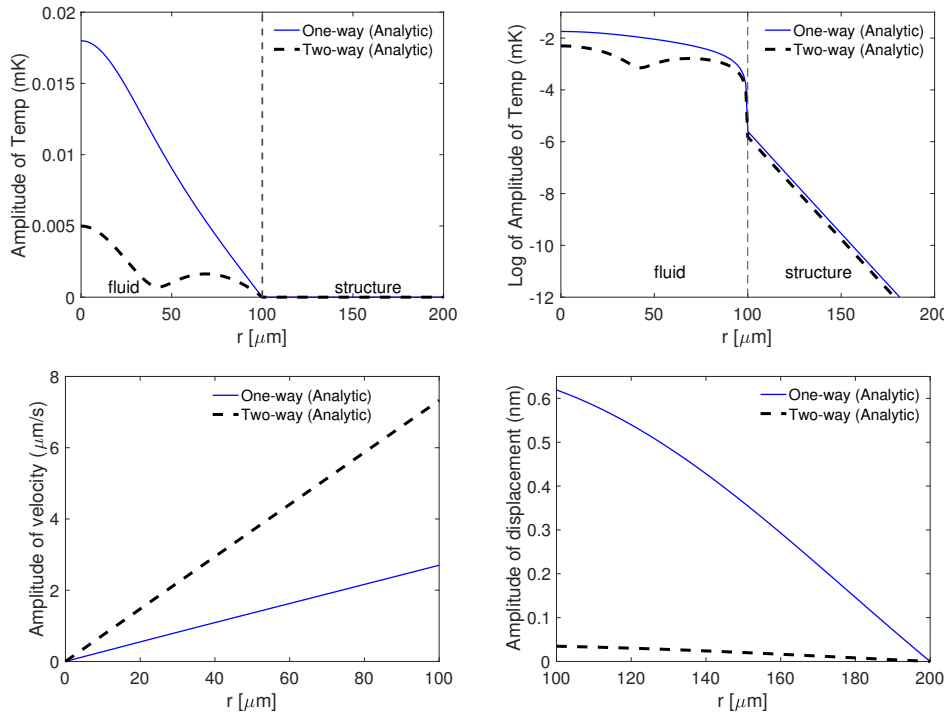


FIG. 6. Comparison of the results obtained with the one-way and two-way coupled models at an atmospheric pressure of 5 Torr.

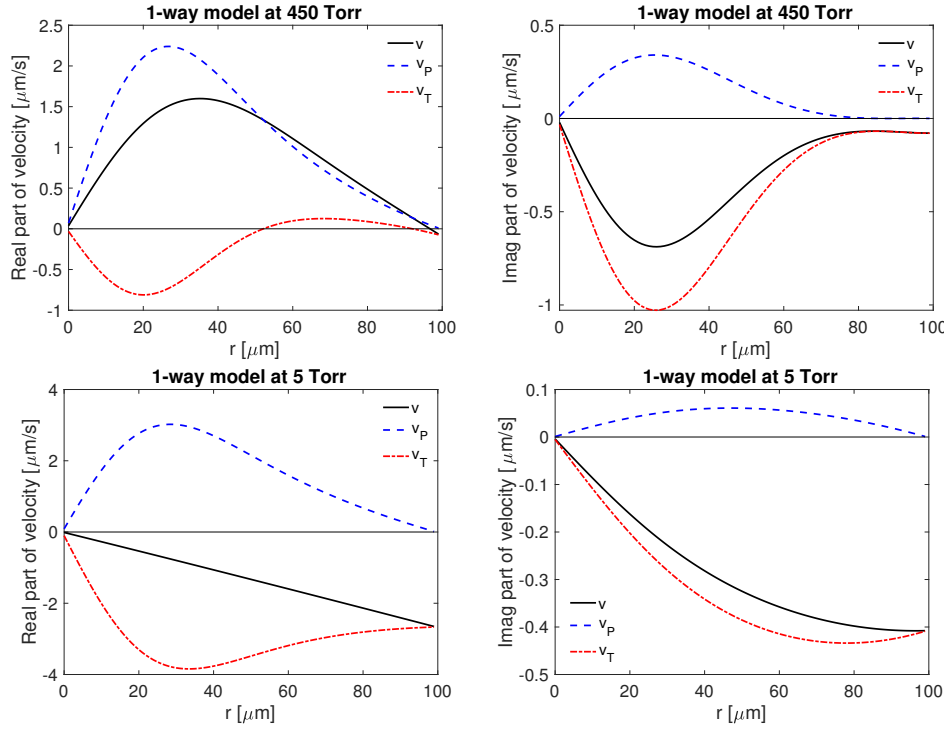


FIG. 7. The acoustic part,  $v_P$ , (dashed blue) and thermal part,  $v_T$ , (dot-dashed red) of the fluid velocity,  $v$ , (solid black) obtained using the one-way model. We show the real parts (left column) and imaginary parts (right column) of these functions at an ambient pressure of 450 Torr (top row) and 5 Torr (bottom row).

450 Torr. The velocity is given by the linear combination of the derivatives of the pressure and temperature in (3.6). Due to the radial symmetry in the problem, the velocity is zero at  $r = 0$ . With the two-way model, the velocity increases almost linearly as  $r$  increases and satisfies the interface condition (2.13) with the structural displacement. Similar trends can be seen at lower ambient pressure in Figures 5 and 6.

Although the one-way model does not include the fluid velocity, it can still be computed using (3.6). Significantly, we observe in Figures 4–6 that the fluid velocity behaves very differently with the one-way model than with the two-way model because of the different interface conditions in the two models. To understand these effects, we decompose the fluid velocity as  $v = v_P + v_T$ , where the acoustic and thermal parts of the velocity are given by

$$(4.1) \quad v_P = \frac{1 - i\gamma\Lambda}{i\omega\rho_F} p' \quad \text{and} \quad v_T = \frac{\alpha\gamma\Lambda}{\omega\rho_F} \tau'_F,$$

respectively. In Figures 7 and 8, we plot the real and imaginary parts of  $v_P$ ,  $v_T$ , and  $v$  at 450 Torr (top row) and 5 Torr (bottom row) for the one-way and two-way models, respectively. With the one-way model,  $v_P = 0$  at the fluid-structure interface, because the condition  $p' = 0$  is imposed there. Consequently, at the interface,  $v$  is determined by the temperature gradient. On the other hand, with the two-way model, at the interface the condition  $v = -i\omega u$  holds and, especially at 450 Torr,  $v_P$  dominates over  $v_T$ . In the fluid domain, even though the pressure is approximately constant and the temperature ranges over several orders of magnitude (see Figures 4–6), except for the

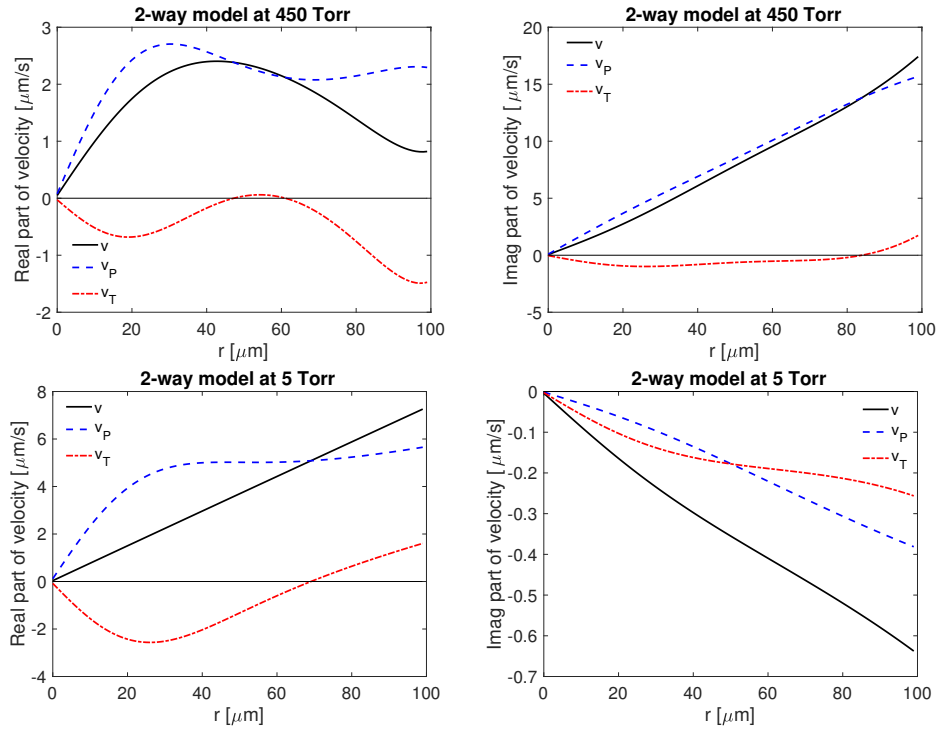


FIG. 8. The acoustic and thermal parts of the fluid velocity obtained using the two-way model.

two-way model at 450 Torr, the acoustic and thermal parts of the fluid velocity are of the same order of magnitude. In particular, in the region of the fluid domain where the source is larger ( $r < 40\mu\text{m}$ ), we observe some destructive interference between  $v_P$  and  $v_T$ . Similar destructive interference effects between the acoustic and thermal components of the signal have been observed in laboratory experiments of trace gas sensors operating at low ambient pressure when the source is positioned very close to the tuning fork [22].

Next we examine the different effects that damping has in the two models. In both models, the resonant vibration of the structure is forced by the pressure and temperature terms in the displacement equation (2.9) and in the corresponding interface condition (2.16). Inspecting the relative sizes of the various terms in these equations, we find that for the simulation results in this paper the temperature-induced forcing is several orders of magnitude smaller than the pressure-induced forcing. In addition to the forcing terms, the equations in the two-way model include other terms that collectively model the damping of the structure due to viscous and thermal effects. In the special case of annular geometry, these are the terms in the interface condition (2.16) for the displacement that involve the viscous stress tensor,  $\sigma_F$ , and the terms in the interface equation (3.3) for pressure and temperature that involve the small viscosity coefficient,  $\Lambda$ . For the simulation results in this paper, at 50 Torr and above,  $\sigma_F$  is about four orders of magnitude smaller than the terms in (2.16) involving  $p$  and  $\mathbf{u}$ , and at 5 Torr it is about two orders of magnitude smaller. On the other hand, in the interface condition (3.3) that relates the gradients of the pressure and temperature to the displacement, all three terms are of the same order of magnitude

at 5 Torr and 50 Torr, while at 450 Torr, the temperature term is about 10% of the pressure and displacement terms. Therefore, this interface condition appears to play the dominant role in damping the vibration of the annular structure.

With the one-way model, damping is instead incorporated using a single parameter in the displacement equation that is chosen so that the resonance width is the same as in the two-way model. However, since there is no a priori reason why the height-to-width ratio of the resonances should be the same for these two very different models, there is no reason why the signal strengths should be the same. In particular, with the one-way model the damping is evenly distributed over the entire structure rather than being concentrated on the boundary of the structure, which could account for the slightly larger signal in the one-way model at ambient pressures above 100 Torr. In addition, as we observed at the end of the previous paragraph, at low ambient pressure the damping effect in the two-way model is more strongly influenced by thermal effects. We therefore suggest that the rapid increase in the signal as the ambient pressure decreases from 100 Torr to 5 Torr is due to the inability of the one-way model to adequately capture the damping effects present in the two-way model at low ambient pressure. Indeed, in their one-way coupled model of a ROTADE sensor with a QTF, Safin, Zweck, and Minkoff [39] encountered similar issues. Specifically, at low ambient pressure they were only able to obtain agreement with laboratory experiments by introducing an ad hoc complex-valued scaling parameter (that depends on the ambient pressure) to adjust the relationship between the acoustic and thermal components of the signal. The different amplitude and phase relationships between  $v_P$  and  $v_T$  that we observed for the one-way model in Figure 7 as compared to the two-way model in Figure 8 suggest that this lack of agreement with the experiment may also be partly due to the simplified nature of the damping in the one-way model.

We conclude this discussion by noting the excellent agreement shown in Figures 4 and 5 between the analytical solutions (dashed black line) and the finite element solutions (solid red line) of the two-way coupled model. We verified that this agreement holds not only for the amplitudes of the dependent variables, but also for their phases.

**5. Conclusion.** In this paper we developed the first model of photoacoustic trace gas sensors involving a two-way coupled system of fluid-structure equations. The periodic interaction between a laser and a trace gas generates thermal and acoustic waves in a viscous fluid. Under suitable operating conditions, these waves excite a resonant vibration in a mechanical structure such as a QTF. This vibrational energy is then converted to an electrical signal whose strength is proportional to the concentration of the trace gas. Our model is based on two subsystems of Helmholtz equations, one for the temperature, pressure, and velocity in the fluid and the other for the temperature and displacement of the structure. These two subsystems are coupled via interface conditions on the structure due to the fluid and on the fluid due to the structure. The novelty of the model is that the signal strength is computed solely in terms of the material parameters of the fluid and structure and the geometry of the structure. In particular, the viscous damping of the structure due to its motion in the fluid is incorporated into the model via thermal and viscous material parameters in the fluid equations and via the two-way coupling at the fluid-structure interface. This feature of the model represents a major advance over prior one-way coupled models in which damping was incorporated in an ad hoc manner using measured values of the  $Q$ -factor of particular experimental systems. Consequently, unlike the one-way coupled model, the two-way model has the potential to enable researchers to increase the sensitivity

of QEPAS sensors by numerically optimizing the geometry of the system, including the dimensions of the QTF and the design and positioning of the microresonator tubes.

To compare the two-way coupled model to an existing one-way model, we derived an analytic solution in the special case of a radially symmetric domain. Even when the  $Q$ -factor of the system is known, one-way models do not always reproduce experimental results, especially at low ambient pressures. We performed a detailed comparison of the one-way and two-way coupled models that identifies deficiencies in the one-way model at low ambient pressures, at least in the special case that the structure is an annulus. To summarize, at higher ambient pressures good agreement has been obtained between experiments and one-way coupled models with the tuning fork geometry, and between the one-way and two-way coupled models with the annular geometry. On the other hand, at low ambient pressure and in other situations where visco-thermal effects play a prominent role, it has not been possible to obtain agreement between experiments and the one-way model with the tuning fork geometry, nor between the two models with the annular geometry. Because the two-way coupled model more accurately incorporates the physics of viscous damping and because of the more realistic predictions of the model at low ambient pressure, we expect that the two-way coupled model will give a better match with experiments than the one-way coupled model. To determine whether or not this is the case we will need to perform fully three-dimensional finite element simulations with a QTF structure and compare the results with those obtained from previously published experiments. However, the computational cost of such two-way model simulations can be quite large due to the need for accurate computations near the fluid-structure interface. To address this issue, we will need to employ custom preconditioners [37] together with a more efficient approach to domain truncation than the perfectly matched layers method used in [38]. One promising approach developed by Kirby, Klöckner, and Sepanski [20] adapts a new nonlocal boundary condition for the domain truncation of Helmholtz equations.

**Appendix A. Finite element discretization.** We derive a finite element implementation of the two-way coupled model discussed in section 2.2. A similar approach has been taken for the one-way coupled model [35, 38, 39].

We reformulate the pressure-temperature subsystem by using (2.1) to eliminate  $\Delta\tau_F$  from (2.2), which we expect will simplify the theoretical analysis of the finite element preconditioners for the system [19]. This gives

$$(A.1) \quad \xi\Delta P + a_1P + a_2\tau_F = ia_3S.$$

$$(A.2) \quad K_F\Delta\tau_F + ib_2\tau_F - ib_1P = -b_3S.$$

Here  $\xi = 1 - i\gamma k\ell_v$ , with  $k = \frac{\omega}{c}$ , and the remaining constants are given by

$$(A.3) \quad \begin{aligned} a_1 &= k^2 \left( \gamma - \frac{\ell_v}{\ell_h}(\gamma - 1) \right), & a_2 &= k^2\gamma\alpha \left( \frac{\ell_v}{\ell_h} - 1 \right), & a_3 &= \frac{\gamma\alpha k^2}{\omega} \frac{\ell_v}{\ell_h}, \\ b_1 &= \rho_F C_p \frac{\omega(\gamma - 1)}{\gamma\alpha}, & b_2 &= \omega\rho_F C_p, & b_3 &= \rho_F C_p. \end{aligned}$$

We also rewrite the linearized Navier–Stokes equations (2.12) as

$$(A.4) \quad i\omega\rho_F \mathbf{v} + \nabla \cdot \boldsymbol{\sigma}_F - \nabla p = \mathbf{0},$$

where the viscous stress tensor is given by

$$(A.5) \quad \boldsymbol{\sigma}_F(\mathbf{v}) = \mu_F \mathbf{E}(\mathbf{v}) + (\eta_F - \frac{2}{3}\mu_F) (\nabla \cdot \mathbf{v}) \mathbf{I}, \quad \text{where } \mathbf{E}(\mathbf{v}) = \frac{1}{2} [\nabla \mathbf{v} + \nabla \mathbf{v}^T].$$

We solve for  $(p, \tau_F, \mathbf{v})$  on  $\Omega_F$  in the product of Sobolev spaces  $\mathcal{W}_F = \mathcal{H}^1(\Omega_F) \times \mathcal{H}^1(\Omega_F) \times [\mathcal{H}^1(\Omega_F)]^3$ , and for  $(\tau_S, \mathbf{u})$  on  $\Omega_S$  in the space  $\mathcal{W}_S = \mathcal{H}^1(\Omega_S) \times [\mathcal{H}^1(\Omega_S)]^3$ . We denote the test functions on these spaces by  $(\phi, \psi, \mathbf{q}) \times (\zeta, \mathbf{w}) \in \mathcal{W}_F \times \mathcal{W}_S$  and we let  $\langle \cdot, \cdot \rangle$  be the standard  $L^2$  inner product. We let  $\mathbf{n}_F$  and  $\mathbf{n}_S = -\mathbf{n}_F$  be the outward unit normal vector fields to the fluid and structure on  $\partial\Omega_{FS}$ .

To derive the variational form of the pressure equation (A.1), we multiply  $p$  by the test function,  $\phi$ , and apply Green's first identity and (3.3) to obtain

$$(A.6) \quad \begin{aligned} & -\xi \langle \nabla p, \nabla \phi \rangle + a_1 \langle p, \phi \rangle + a_2 \langle \tau_F, \phi \rangle \\ & = ia_3 \langle S, \phi \rangle + i\gamma\alpha k\ell_v \int_{\partial\Omega_{FS}} (\nabla \tau_F \cdot \mathbf{n}_F) \phi \, dA - \omega^2 \rho_F \int_{\partial\Omega_{FS}} (\mathbf{u} \cdot \mathbf{n}_F) \phi \, dA. \end{aligned}$$

Similarly, the variational form of the temperature equation (A.2) is

$$(A.7) \quad \begin{aligned} & -K_F \langle \nabla \tau_F, \nabla \psi \rangle - ib_1 \langle p, \psi \rangle + ib_2 \langle \tau_F, \psi \rangle \\ & = -b_3 \langle S, \psi \rangle + \int_{\partial\Omega_{FS}} [K_S \nabla \tau_S] \cdot \mathbf{n}_S \psi \, dA, \end{aligned}$$

and the variational form of the heat equation (2.5) in the structure is given by

$$(A.8) \quad -\langle K_S \nabla \tau_S, \nabla \zeta \rangle + i\omega \rho_S C_{p,S} \langle \tau_S, \zeta \rangle = K_F \int_{\partial\Omega_{FS}} (\nabla \tau_F \cdot \mathbf{n}_F) \zeta \, dA.$$

The variational form of the fluid velocity equation (A.4) is

$$(A.9) \quad \langle \nabla \cdot \boldsymbol{\sigma}_F, \mathbf{q} \rangle + i\omega \rho_F \langle \mathbf{v}, \mathbf{q} \rangle - \langle \nabla p, \mathbf{q} \rangle = \mathbf{0}.$$

Next, we recall that when the divergence theorem is applied to a vector field of the form  $\mathbf{Av}$ , where  $\mathbf{A}$  is a symmetric matrix-valued function, we obtain the integration by parts formula

$$(A.10) \quad \langle \nabla \cdot \mathbf{A}, \mathbf{v} \rangle = -\langle \mathbf{A} : \mathbf{E}(\mathbf{v}) \rangle + \int_{\partial\Omega} (\mathbf{A}\mathbf{n}) \cdot \mathbf{v} \, dA,$$

where  $\langle \mathbf{A} : \mathbf{B} \rangle = \int_{\Omega} \text{Tr}[\mathbf{A}(\mathbf{x})\mathbf{B}^*(\mathbf{x})] \, d\mathbf{x}$ . Consequently, (A.9) is equivalent to

$$(A.11) \quad -i\omega \rho_F \langle \mathbf{v}, \mathbf{q} \rangle + \langle \boldsymbol{\sigma}_F : \mathbf{E}(\mathbf{q}) \rangle - \langle p, \nabla \cdot \mathbf{q} \rangle = \int_{\partial\Omega_{FS}} (\boldsymbol{\sigma}_F \mathbf{n}_F) \cdot \mathbf{q} \, dA - \int_{\partial\Omega_{FS}} p(\mathbf{n}_F \cdot \mathbf{q}) \, dA.$$

Then, by (2.16) the variational form of the Navier–Stokes equation (2.12) is given by

$$(A.12) \quad -i\omega \rho_F \langle \mathbf{v}, \mathbf{q} \rangle + \langle \boldsymbol{\sigma}_F : \mathbf{E}(\mathbf{q}) \rangle - \langle p, \nabla \cdot \mathbf{q} \rangle = \int_{\partial\Omega_S^{\text{Free}}} (\mathbf{C}[\boldsymbol{\alpha}_s \tau_S] - \mathbf{C}[\mathbf{E}(\mathbf{u})]) \mathbf{n}_S \cdot \mathbf{q} \, dA.$$

Similarly, by (2.9), (2.16), and (A.10), the weak form of the elasticity equation is

$$(A.13) \quad \begin{aligned} -\langle \mathbf{C}[\mathbf{E}(\mathbf{u})] : \mathbf{E}(\mathbf{w}) \rangle + \rho_S \omega^2 \langle \mathbf{u}, \mathbf{w} \rangle & = -\langle \mathbf{C}[\boldsymbol{\alpha}_s \tau_S] : \mathbf{E}(\mathbf{w}) \rangle \\ & - \int_{\partial\Omega_S^{\text{Free}}} p(\mathbf{n}_F \cdot \mathbf{w}) \, dA + \int_{\partial\Omega_S^{\text{Free}}} (\boldsymbol{\sigma}_F \mathbf{n}_F) \cdot \mathbf{w} \, dA. \end{aligned}$$

As we explained in subsection 3.1, in the special case of the annular geometry, the no-penetration, no-slip interface condition (2.13) is already enforced in (A.6) since in this case (2.13) is equivalent to (3.3). For general geometry, Safin [37] shows how to impose (2.13) by adapting the methods described in [6, 16, 36] for imposing additional continuity conditions. The matrix formulation of the variational equations above is also given in the Ph.D. thesis of Safin [37].

**Acknowledgment.** We thank an anonymous reviewer for several suggestions that significantly improved the paper.

## REFERENCES

- [1] G. AOUST, R. LEVY, B. BOURGETEAU, AND O. LE TRAON, *Viscous damping on flexural mechanical resonators*, *Sens. Actuators A: Phys.*, 230 (2015), pp. 126–135.
- [2] G. AOUST, R. LEVY, B. BOURGETEAU, AND O. LE TRAON, *Acoustic damping on flexural mechanical resonators*, *Sens. Actuators A: Phys.*, 238 (2016), pp. 158–166.
- [3] G. AOUST, R. LEVY, M. RAYBAUT, A. GODARD, J.-M. MELKONIAN, AND M. LEFEBVRE, *Theoretical analysis of a resonant quartz-enhanced photoacoustic spectroscopy sensor*, *Appl. Phys. B*, 123 (2017), 63.
- [4] A. P. FRENCH, *Vibrations and Waves*, W. W. Norton & Company, New York, 1971.
- [5] B. BRENNAN AND R. C. KIRBY, *Finite element approximation and preconditioners for a coupled thermal-acoustic model*, *Comput. Math. Appl.*, 70 (2015), pp. 2342–2354.
- [6] E. BURMAN AND M. FERNÁNDEZ, *Explicit strategies for incompressible fluid-structure interaction problems: Nitsche type mortaring versus Robin-Robin coupling*, *Internat. J. Numer. Methods Engrg.*, 97 (2013), pp. 739–758.
- [7] Y. CAO AND G. J. DIEBOLD, *Effects of heat conduction and viscosity on photoacoustic waves from droplets*, *Opt. Eng.*, 36 (1997), pp. 417–422.
- [8] D. CARLSON, *Linear thermoelasticity*, in *Linear Theories of Elasticity and Thermoelasticity: Linear and Nonlinear Theories of Rods, Plates, and Shells*, C. Truesdell, ed., Springer-Verlag, Berlin, Heidelberg, 1973, pp. 273–345.
- [9] A. J. CHORIN AND J. E. MARSDEN, *A Mathematical Introduction to Fluid Mechanics*, Springer-Verlag, New York, 1979.
- [10] J. CORDIOLI, G. MARTINS, P. MAREZE, AND R. JORDAN, *A comparison of models for visco-thermal acoustic problems*, in *InterNoise 10*, International Institute of Noise Control Engineering, 2010, pp. 6992–7001.
- [11] R. COX, J. ZHANG, F. JOSSE, S. M. HEINRICH, I. DUFOUR, L. A. BEARDSLEE, AND O. BRAND, *Damping and mass sensitivity of laterally vibrating resonant microcantilevers in viscous liquid media*, in *2011 Joint Conference of the IEEE International Frequency Control and the European Frequency and Time Forum (FCS) Proceedings*, 2011, pp. 1–6.
- [12] L. DONG, A. A. KOSTEREV, D. THOMAZY, AND F. K. TITTEL, *QEPAS spectrophones: Design, optimization, and performance*, *Appl. Phys. B*, 100 (2010), pp. 627–635.
- [13] M. DUQUESNOY, G. AOUST, J.-M. MELKONIAN, R. LÉVY, M. RAYBAUT, AND A. GODARD, *Quartz enhanced photoacoustic spectroscopy based on a custom quartz tuning fork*, *Sensors*, 19 (2019), p. 1362.
- [14] S. L. FIREBAUGH, A. SAMPAOLO, P. PATIMISCO, V. SPAGNOLO, AND F. K. TITTEL, *Modeling the dependence of fork geometry on the performance of quartz enhanced photoacoustic spectroscopic sensors*, in *2015 Conference on Lasers and Electro-Optics (CLEO)*, 2015, ATu1J.3.
- [15] S. L. FIREBAUGH, E. A. TERRAY, AND L. DONG, *Optimization of resonator radial dimensions for quartz enhanced photoacoustic spectroscopy systems*, in *Proc. SPIE 8600, Laser Resonators, Microresonators, and Beam Control XV*, 2013, 86001S.
- [16] L. GERARDO-GIORDA, F. NOBILE, AND C. VERGARA, *Analysis and optimization of Robin–Robin partitioned procedures in fluid-structure interaction problems*, *SIAM J. Numer. Anal.*, 48 (2010), pp. 2091–2116, <https://doi.org/10.1137/09076605X>.
- [17] N. JOLY, M. BRUNEAU, AND R. BOSSART, *Coupled equations for particle velocity and temperature variation as the fundamental formulation of linear acoustics in thermo-viscous fluids at rest*, *Acta Acust United Acustica*, 92 (2006), pp. 202–209.
- [18] J. KADERLI, J. ZWECK, A. SAFIN, AND S. MINKOFF, *An analytic solution to the coupled pressure-temperature equations for modeling of photoacoustic trace gas sensors*, *J. Engrg. Math.*, 103 (2017), pp. 173–193.
- [19] R. C. KIRBY AND P. COOGAN, *Optimal-order preconditioners for the Morse-Ingard equations*, *Comput. Math. Appl.*, 79 (2020), pp. 2458–2471.
- [20] R. C. KIRBY, A. KLÖCKNER, AND B. SEPANSKI, *Finite elements for Helmholtz equations with a nonlocal boundary condition*, *SIAM J. Sci. Comput.*, 43 (2021), pp. A1671–A1691, <https://doi.org/10.1137/20M1368100>.
- [21] A. KOSTEREV, Y. BAKHIRKIN, R. CURL, AND F. TITTEL, *Quartz-enhanced photoacoustic spectroscopy*, *Opt. Lett.*, 27 (2002), pp. 1902–1904.
- [22] A. A. KOSTEREV AND J. H. DOTY III, *Resonant optothermoacoustic detection: Technique for measuring weak optical absorption by gases and micro-objects*, *Opt. Lett.*, 35 (2010), pp. 3571–3573.

- [23] A. A. KOSTEREV AND F. K. TITTEL, *Ammonia detection by use of quartz-enhanced photoacoustic spectroscopy with a near-IR telecommunication diode laser*, Appl. Opt., 43 (2004), pp. 6213–6217.
- [24] A. A. KOSTEREV, F. K. TITTEL, D. V. SEREBRYAKOV, A. L. MALINOVSKY, AND I. V. MOROZOV, *Applications of quartz tuning forks in spectroscopic gas sensing*, Rev. Sci. Instruments, 76 (2005), 043105.
- [25] L. D. LANDAU AND E. M. LIFSHITZ, *Fluid Mechanics*, Addison-Wesley Publishing Company, Reading, MA, 1959.
- [26] T. LAVERGNE, N. JOLY, AND S. DURAND, *Acoustic thermal boundary condition on thin bodies: Application to membranes and fibres*, Acta Acust United Acustica, 99 (2013), pp. 524–536.
- [27] K. LIU, X. GUO, H. YI, W. CHEN, W. ZHANG, AND X. GAO, *Off-beam quartz-enhanced photoacoustic spectroscopy*, Opt. Lett., 34 (2009), pp. 1594–1596.
- [28] A. MIKLÓS, S. SCHÄFER, AND P. HESS, *Photoacoustic spectroscopy, theory*, in Encyclopedia of Spectroscopy and Spectrometry, J. C. Lindon, G. E. Tranter, and J. L. Holmes, eds., Vol. 3, Academic Press, 2000, pp. 1815–1822.
- [29] T. MILDE, M. HOPPE, H. TATENGUEM, M. MORDMÜLLER, J. O'GORMAN, U. WILLER, W. SCHADE, AND J. SACHER, *QEPAS sensor for breath analysis: A behavior of pressure*, Appl. Opt., 57 (2018), pp. C120–C127.
- [30] P. M. MORSE AND K. U. INGARD, *Theoretical Acoustics*, Princeton University Press, Princeton, NJ, 1986.
- [31] W. E. NEWELL, *Miniatrurization of tuning forks*, Science, 161 (1968), pp. 1320–1326.
- [32] P. PATIMISCO, A. SAMPAOLO, L. DONG, F. K. TITTEL, AND V. SPAGNOLO, *Analysis of the electro-elastic properties of custom quartz tuning forks for optoacoustic gas sensing*, Sens. Actuators B: Chem., 227 (2016), pp. 539–546.
- [33] P. PATIMISCO, A. SAMPAOLO, L. DONG, F. K. TITTEL, AND V. SPAGNOLO, *Recent advances in quartz enhanced photoacoustic sensing*, Appl. Phys. Rev., 5 (2018), 011106.
- [34] N. PETRA, J. ZWECK, A. KOSTEREV, S. MINKOFF, AND D. THOMAZY, *Theoretical analysis of a quartz-enhanced photoacoustic spectroscopy sensor*, Appl. Phys. B, 94 (2009), pp. 673–680.
- [35] N. PETRA, J. ZWECK, S. E. MINKOFF, A. A. KOSTEREV, AND J. H. DOTY III, *Modeling and design optimization of a resonant optothermoacoustic trace gas sensor*, SIAM J. Appl. Math., 71 (2011), pp. 309–332, <https://doi.org/10.1137/100807181>.
- [36] A. QUARTERONI AND A. VALLI, *Domain Decomposition Methods for Partial Differential Equations*, Oxford Science Publications, The Clarendon Press, Oxford University Press, New York, 1999.
- [37] A. SAFIN, *Modeling Trace Gas Sensors with the Coupled Pressure-Temperature Equations*, Ph.D. thesis, The University of Texas at Dallas, 2018.
- [38] A. SAFIN, S. MINKOFF, AND J. ZWECK, *A preconditioned finite element solution of the coupled pressure-temperature equations used to model trace gas sensors*, SIAM J. Sci. Comput., 40 (2018), pp. B1470–B1493, <https://doi.org/10.1137/17M1145823>.
- [39] A. SAFIN, J. ZWECK, AND S. E. MINKOFF, *A one-way coupled model for the vibration of tuning fork-based trace gas sensors driven by a thermoacoustic wave*, Appl. Phys. B, 126 (2020), 29.
- [40] I. N. SNEDDON, *The Linear Theory of Thermoelasticity*, University of Glasgow, Springer-Verlag, 1974.
- [41] S. SOLGA, T. SCHWARTZ, M. MUDALEL, L. SPACEK, R. LEWICKI, F. TITTEL, C. LOCCIONI, AND T. RISBY, *Factors influencing breath ammonia determination*, J. Breath Res., 7 (2013), 037101.
- [42] F. TITTEL AND R. LEWICKI, *Tunable mid-infrared laser absorption spectroscopy*, in Semiconductor Lasers: Fundamentals and Applications, A. Baranov and E. Tournie, eds., Woodhead Publishing Ltd, 2013, pp. 579–629.